Transient Unsaturated Seepage and Stability of a Homogeneous Earth Dam: A Case Study

Yihan Yu*, Bingkuo Song

School of Water Conservancy, North China University of Water Resources and Electric Power, Zhengzhou, Henan, China

*Corresponding author: 1337232981@qq.com

Abstract. Rapid reservoir level fluctuations drive transient seepage evolution in earth dams and induce redistribution of stress and deformation, thereby affecting slope stability. This study investigates a homogeneous earth dam in a small reservoir using a two-dimensional finite element model. Transient seepage in unsaturated media is simulated with a governing formulation parameterised by the van Genuchten soil-water retention relationship, and stability is evaluated using the strength reduction method based on the seepage results. Three representative scenarios are considered: the normal water level (108.5 m), rapid drawdown (108.5 m to 101.0 m at 0.5 m/d), and storm-driven rapid rise (108.5 m to 109.5 m at 0.5 m/d). During drawdown, pore water pressure along the upstream slope decreases while effective stress within the dam generally increases. Deformation concentrates near the upstream side under drawdown, whereas rapid rise produces a more pronounced downstream displacement response over a broader region. The factor of safety exhibits a non-monotonic trend during drawdown, increasing slightly from 1.92 to 1.96 before dropping rapidly to 1.02 at 101.0 m, with the critical slip surface predominantly developing on the downstream side. The results provide practical implications for reservoir operation and monitoring of small and medium-sized earth dams under rapid water-level changes.

Keywords: earth dam, unsaturated seepage, rapid drawdown, stability evolution

1 Introduction

Earth rockfill dams are among the most widely used dam types worldwide, and their long term performance is closely associated with downstream safety and regional sustainability. Rapid and frequent water level fluctuations modify hydraulic boundary conditions and drive transient seepage evolution with the migration of wetted zones, which in turn alters the mechanical response of the dam body [1]. Understanding this transient evolution is of paramount importance for dam safety, as traditional steady-state evaluations often fail to capture the critical, time-dependent variations in effective stress. In particular, during rapid drawdown, the dissipation of internal pore water pressure fre-

J. Zhang et al. (eds.), *Proceedings of the 2026 2nd International Conference on Engineering Management and Safety Engineering (EMSE 2026)*, Advances in Engineering Research 300,
https://doi.org/10.2991/978-94-6239-703-3_7

quently lags behind the external boundary unloading [2]. This temporal mismatch generates outward-directed seepage forces and severe degradation of the soil skeleton's shear strength. Consequently, localized plastic yielding can rapidly propagate into catastrophic large-scale slope failure. Therefore, elucidating the transient seepage characteristics is not merely a theoretical extension, but a prerequisite for accurate stability assessment and early warning of earth-rockfill dams under extreme operational conditions.

Considerable efforts have been devoted to saturated and unsaturated seepage analysis, transient seepage safety evaluation, and slope stability assessment of earth rockfill dams. Nevertheless, several issues remain insufficiently addressed from the perspective of operational risk control. First, the transient nature of seepage during water level fluctuations implies that stability cannot be reliably evaluated using steady state seepage fields or single field analyses, as seepage lag and wetting front migration may substantially reshape the stability margin [3]. Second, small and medium sized dams often operate under alternating scenarios, such as rapid drawdown followed by storm induced water level rise, calling for a unified framework to compare seepage response, stress deformation behaviour, and stability evolution across representative operating conditions [4]. Third, stability evaluation should be hydraulically consistent with transient seepage computations, otherwise the linkage between numerical results and practical decision making for monitoring and reservoir scheduling may be weakened [5].

In this study, a small reservoir earth rockfill dam is taken as the case study. A two dimensional finite element model is developed in COMSOL Multiphysics, where transient seepage behaviour is described using a governing formulation suitable for unsaturated media together with an appropriate soil water retention relationship. Based on the transient seepage results, slope stability is evaluated using the strength reduction method. Typical operating conditions, including normal water level, rapid drawdown, and storm induced rapid rise, are considered to systematically quantify the evolution of pore water pressure, effective stress, displacement, and plastic development, as well as the corresponding variation of factor of safety (FoS). The findings aim to provide practical insights and a reproducible modelling route for safety evaluation and risk mitigation of small and medium sized earth rockfill dams under complex operating conditions.

2 Methodology

2.1 Seepage Governing Equations

The objective of seepage analysis is to determine the spatial and temporal evolution of pore water pressure or hydraulic head under prescribed reservoir water level loading. This provides the basis to quantify phreatic surface migration, pressure dissipation and lag effects, and to supply consistent hydraulic inputs for subsequent deformation and stability analyses. Darcy law is adopted to describe flow through porous media [6]:

$$\mathbf{q} = -\mathbf{K}\nabla h \tag{1}$$

where **q** is the Darcy flux, **K** is the hydraulic conductivity tensor, and h is the total hydraulic head defined as

$$h = \psi + z \tag{2}$$

with ψ being the pressure head and $z$the elevation head.

The governing equation is obtained from mass conservation:

$$\frac{\partial \theta}{\partial t} + \nabla \cdot \mathbf{q} = Q \tag{3}$$

where θ is the volumetric water content and Q is a source or sink term. Substituting Eq. (1) into Eq. (3) yields the seepage equation in terms of hydraulic head. For steady saturated flow, $\partial\theta / \partial t = 0$, the governing equation becomes

$$\nabla \cdot (\mathbf{K}\nabla h) = Q \tag{4}$$

For an isotropic medium with $\mathbf{K} = K\mathbf{I}$, Eq. (4) reduces to a Laplace type or Poisson type equation:

$$K\nabla^2 h = Q \tag{5}$$

For transient saturated flow driven by reservoir level fluctuations, storage effects are included through the specific storage S_s:

$$S_s \frac{\partial h}{\partial t} = \nabla \cdot (\mathbf{K}\nabla h) + Q \tag{6}$$

Reservoir level changes may generate partially saturated zones due to phreatic surface migration, for which the hydraulic conductivity depends on the moisture state. To represent both saturated and unsaturated behavior, Richards equation in mixed form is adopted [7]:

$$C(\psi)\frac{\partial \psi}{\partial t} = \nabla \cdot [K(\psi)\nabla(\psi + z)] + Q \tag{7}$$

where $C(\psi) = \partial\theta / \partial\psi$ is the specific moisture capacity and $K(\psi)$ is the unsaturated hydraulic conductivity. Closure of Eq. (7) requires a soil water retention relationship and a relative permeability function. The van Genuchten model is used for effective saturation [8]:

$$S_e = \frac{\theta - \theta_r}{\theta_s - \theta_r} = [1 + (\alpha \mid \psi \mid)^n]^{-m}, m = 1 - \frac{1}{n} \tag{8}$$

where θ_s and θ_r are the saturated and residual volumetric water contents, and α, n, m are fitting parameters. The relative permeability is described using the Mualem and van Genuchten function [9]:

$$k_r(S_e) = S_e^l \left[1 - \left(1 - S_e^{1/m}\right)^m\right]^2 \tag{9}$$

and the unsaturated hydraulic conductivity is

$$K(\psi) = K_s\, k_r(S_e) \tag{10}$$

where K_s is the saturated hydraulic conductivity and l is a pore connectivity parameter.

2.2 Coupled Formulation for Seepage and Deformation

The mechanical response of a dam under seepage is governed by the influence of pore water pressure on effective stress and the resulting deformation, while the deformation induced volumetric strain affects fluid storage and pressure evolution. To capture this interaction, a coupled formulation is employed with displacement $\mathbf{u}$ and pore water pressure p as primary variables, solved within the same time increment.

The effective stress concept is expressed in Biot form [10]:

$$\boldsymbol{\sigma} = \boldsymbol{\sigma}' - \alpha\, p\, \mathbf{I} \tag{11}$$

where $\boldsymbol{\sigma}$ is total stress, $\boldsymbol{\sigma}'$ is effective stress, $\alpha$is the Biot coefficient, and $\mathbf{I}$ is the identity tensor. Under quasi static conditions and small strain assumption, equilibrium is written as

$$\nabla \cdot \boldsymbol{\sigma} + \rho \mathbf{b} = \mathbf{0} \tag{12}$$

The strain tensor is defined as

$$\boldsymbol{\varepsilon} = \frac{1}{2}(\nabla \mathbf{u} + (\nabla \mathbf{u})^T) \tag{13}$$

and the constitutive relationship is expressed in a general form

$$\boldsymbol{\sigma}' = \mathbf{D} : \boldsymbol{\varepsilon} \tag{14}$$

where $\mathbf{D}$ denotes the material stiffness operator, which depends on the material model adopted in subsequent sections.

Fluid mass conservation in a deformable porous medium is written as [11]

$$\frac{1}{M}\frac{\partial p}{\partial t} + \alpha \frac{\partial \varepsilon_v}{\partial t} + \nabla \cdot \mathbf{q} = s \tag{15}$$

where M is the Biot modulus, $\varepsilon_v = \mathrm{tr}(\boldsymbol{\varepsilon})$ is volumetric strain, and s is a source term. Darcy law in terms of pore pressure is

$$\mathbf{q} = -\frac{\mathbf{k}}{\mu}(\nabla p - \rho_w \mathbf{g}) \tag{16}$$

where $\mathbf{k}$ is intrinsic permeability, μ is dynamic viscosity, ρ_w is water density, and $\mathbf{g}$ is gravitational acceleration.

The coupled system given by Eqs. (12) to (16) is discretized using the finite element method and solved with a fully coupled implicit scheme in COMSOL Multiphysics [12]. To ensure the transparency and replicability of the numerical modelling, the specific computational procedures are detailed as follows. Prior to the transient analysis, a steady-state geostatic step was executed under the normal water level (108.50 m) to establish a physically consistent initial effective stress field and phreatic surface. For the

subsequent transient simulations, the backward differentiation formula was adopted for time integration, utilizing an adaptive time-stepping strategy. This adaptive approach is crucial for capturing the rapid stress and pore pressure redistributions during the early stages of water-level changes while maintaining computational efficiency later on.

Within each time step, displacement and pore pressure were iteratively updated using a robust highly non-linear Newton-Raphson solver. A direct linear solver was employed to handle the potentially ill-conditioned matrices characteristic of unsaturated soil mechanics. The iteration continued until the predefined relative tolerance criteria for both the fluid mass conservation and mechanical equilibrium residuals were strictly satisfied. This ensures rigorous numerical consistency between the computed pore pressure field and the corresponding effective stress and deformation fields, which is essential for the reliability of the subsequent stability evaluation.

2.3 Stability Evaluation

Slope stability under reservoir level fluctuations is evaluated using the strength reduction method. The shear strength is described by the Mohr-Coulomb criterion [13]:

$$\tau_f = c + \sigma_n' \tan\ \varphi \tag{17}$$

where c is cohesion, φ is the friction angle, and σ_n' is the effective normal stress.

In the strength reduction procedure, the shear strength parameters are reduced by a factor F:

$$c_F = \frac{c}{F} \tag{18}$$

$$\tan\ \varphi_F = \frac{\tan \varphi}{F} \tag{19}$$

The reduction factor is increased progressively until a limit state is reached, and the critical factor is defined as the FoS:

$$\mathrm{FoS} = F_{\mathrm{cr}} \tag{20}$$

Failure is identified based on reproducible numerical indicators, including inability to satisfy convergence criteria, a clear acceleration of displacement at key monitoring points, and the formation of a continuous band of equivalent plastic strain. The pore pressure field used in the strength reduction analysis is taken from the coupled seepage deformation calculation and incorporated through the effective stress relationship in Eq. (11), ensuring hydraulic and mechanical consistency.

3 Case Study and Numerical Model Setup

3.1 Overview of the Reservoir

The reservoir is classified as a small Type I project.The normal water level is 108.50 m, while the check flood level is 109.50 m (probability = 2%). The hydraulic system

mainly consists of a homogeneous earth rockfill dam, an open spillway, and a horizontal culvert. For the maximum cross-section, the dam height is 26 m, with a crest width of 5 m and a base width of 137 m. The crest elevation and foundation elevation are 110.50 m and 84.50 m, respectively.

3.2 Coupled Numerical Modelling of the Dam

To investigate the seepage response, stress deformation behaviour, and stability evolution under reservoir level fluctuations and storm-induced scenarios, a two-dimensional finite element model was established based on the maximum cross-section of the dam. Considering that the influence of bedrock on seepage and slope stability is relatively limited for the present problem, the bedrock layer was not included in the computational domain. The model domain comprises the dam body and a 9 m thick clay foundation layer. The foundation clay was discretised using mapped meshes, whereas the dam body was discretised using free quadrilateral elements. The final mesh contains 2993 domain elements and 594 boundary elements, and the mesh configuration is given in Fig. 2. The model geometry together with the monitoring points is provided in Fig. 1.

For the seepage analysis, the upstream boundary was prescribed as a time-dependent reservoir head. On the downstream side, a constant-head boundary was applied below the downstream water level, while a seepage-face condition was assigned to the downstream slope surface above the water level. To track the pore water pressure response along the upstream slope during water-level changes, three monitoring points (Points A, B, and C) were arranged on the upstream slope surface. To capture the stress variation within the dam body, four interior monitoring points (Points D, E, F, and G) were defined inside the dam. All coordinates follow the coordinate system shown in Fig. 1. Specifically, Points A, B, and C are located at (115, 105), (105, 100), and (95, 95), respectively, while Points D, E, F, and G are located at (133, 110), (133, 100), (133, 90), and (128, 105), respectively.

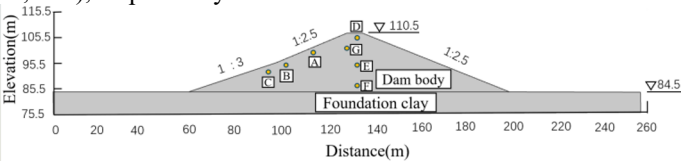

Fig. 1. Dam calculation model and survey point layout map.

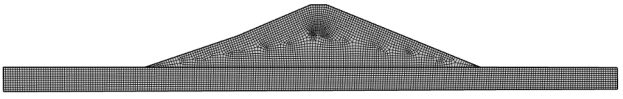

Fig. 2. Grid division map.

The computational domain includes two materials, namely the dam material and the clay foundation. According to the engineering geological data, the unit weight γ, effective cohesion c', effective friction angle φ', and saturated hydraulic conductivity k_s are listed in Table 1. For saturated and unsaturated seepage analysis, the dam material was

characterised using the van Genuchten model to describe the relationship between volumetric water content and matric suction. The parameters were set as $\theta_s = 0.43$ and $\theta_r = 0.05$, with $\alpha = 6.65$ kPa, $n = 2.68$, and $m = 0.63$. The foundation clay remains below the water level and was treated as a saturated material.

Table 1. Parameters of materials for dam and foundation

Parameters	Material Type	
	Foundation clay	***Dam body materials***
φ' (°)	21.8	23
k_s (m/s)	1.6×10^{-4}	1.0×10^{-5}
c' (kPa)	180	15
γ (kN/m^3)	19.3	20.5

Three representative operational scenarios were considered, including the normal water level, rapid drawdown, and storm-induced rapid rise. The drawdown scenario assumes that the reservoir level decreases uniformly from 108.50 m to 101.00 m, corresponding to a total drawdown magnitude of $H = 7.5$ m, with a drawdown rate of $v = 0.5$ m/d. This scenario is used to examine the evolution of pore water pressure, stress, displacement, and plastic development, and to evaluate the stability response. In addition, flood-related conditions at high water levels were analysed, including a rapid-rise scenario driven by rainfall, with a rise rate of $v = 0.5$ m/d. The downstream water level was fixed at 85.50 m for all cases.

4 Results and Discussion

4.1 Responses of Pore Water Pressure and Effective Stress

When the reservoir level drops to 101 m, the distributions of pore water pressure and effective stress are summarized in Fig. 3. A depth-dependent pore-pressure pattern can be observed from Fig. 3(a). Pore water pressure increases from the shallow zone toward the deeper part of the dam, with relatively high values concentrated in the lower central region and a gradual decrease toward both slopes. The corresponding effective stress field, provided in Fig. 3(b), exhibits an opposite tendency in terms of mechanical significance: higher effective stress tends to concentrate in the dam interior, whereas the near-surface slope region remains comparatively low. Together, the two contour maps indicate that the mechanical state during drawdown cannot be interpreted from a single field alone, because the hydraulic response directly affects the effective stress distribution.

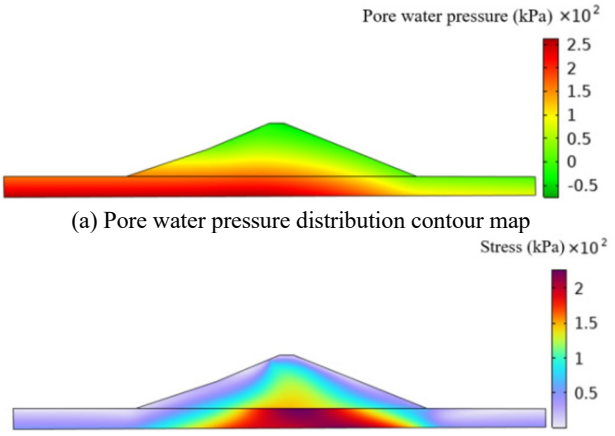

(a) Pore water pressure distribution contour map

(b) Effective stress distribution contour map

Fig. 3. Contours at the reservoir level of 101 m: (a) pore water pressure (kPa) and (b) effective stress (kPa). The upstream and downstream directions are indicated in Fig. 1. The colour bars represent the magnitude of each field.

The evolution at monitoring points further clarifies the drawdown response. As illustrated in Fig. 4(a), pore water pressure at Points A, B, and C decreases progressively with the reservoir level. Meanwhile, an overall increase in effective stress is evident at the interior points in Fig. 4(b). This trend is consistent with pore-pressure dissipation, which leads to an increased stress share carried by the soil skeleton.

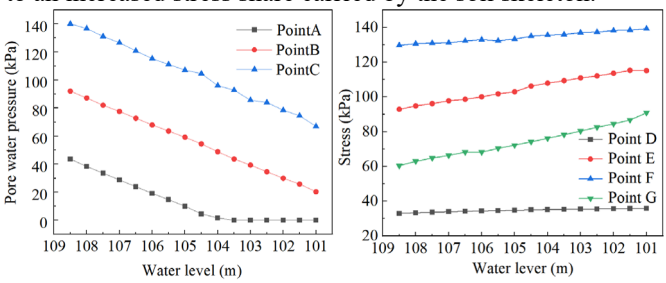

(a) (b)

Fig. 4. Variation curves of pore water pressure and effective stress at different observation points under varying reservoir water levels.

The role of drawdown rate should also be emphasized. If pore pressure dissipation inside the dam is slower than the external water-level reduction, relatively high pore pressure may persist within the dam body even after the upstream hydrostatic support has been removed. Under such conditions, the hydraulic boundary unloading and the internal pressure redistribution become temporally mismatched, which may promote unfavorable stress states and deformation tendencies. Therefore, drawdown safety should be evaluated using the computed pore-pressure evolution together with the associated effective-stress redistribution.

4.2 Displacement Characteristics under Drawdown and Rise

The displacement response under drawdown is quantified at upstream monitoring points in Fig. 5. It can be observed that displacement increases as the reservoir level decreases. In addition, the displacement change becomes more pronounced at higher elevations, suggesting that the upper part of the upstream slope is more sensitive to water-level variation. This behavior is closely linked to seepage redistribution during drawdown. In particular, when phreatic surface migration inside the dam lags behind the external boundary change, outward seepage develops and generates seepage forces directed toward the outside of the dam, which can intensify outward deformation near the upstream slope.

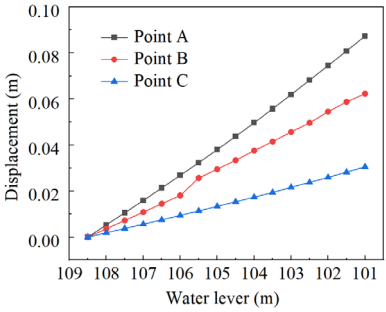

Fig. 5. Displacement variation curves at each observation point at different reservoir water levels.

A direct comparison between drawdown and rise scenarios is provided by the displacement contours in Fig. 6. Under drawdown, deformation concentrates mainly on the upstream side, as evidenced by Fig. 6(a), whereas deformation elsewhere remains limited. In contrast, the rise scenario produces a clearer displacement response toward the downstream side and affects a broader region, as indicated in Fig. 6(b). This difference suggests that water-level rise expands the wetted region and modifies the seepage field over a larger domain, thereby triggering deformation responses in a wider portion of the dam body.

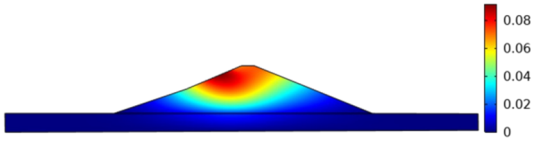

(a) Water level decline chart (Water level at 101m)

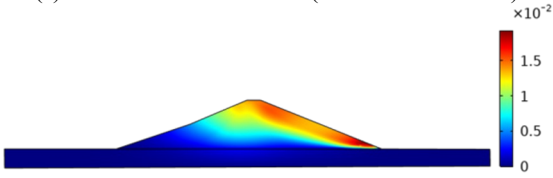

(b) Water level rise chart (Water level at 109.5m)

Fig. 6. Displacement contours under different operational scenarios: (a) rapid drawdown to 101 m and (b) rapid rise to 109.5 m. The colour bar denotes displacement magnitude.

Overall, drawdown and rise lead to distinct deformation locations and influence ranges, which has practical implications for monitoring design and for identifying critical zones under different operational conditions.

4.3 Stability Evaluation

The plastic deformation pattern at the normal reservoir level is evaluated first. Under the normal water level of 108.5 m, the critical-state equivalent plastic strain distribution is given in Fig. 7, and the corresponding factor of safety is FoS = 1.92. With increasing strength reduction, the plastic zone initiates near the toe region and progressively extends toward the dam interior, reflecting strain localization and the emergence of a potential shear band at failure.

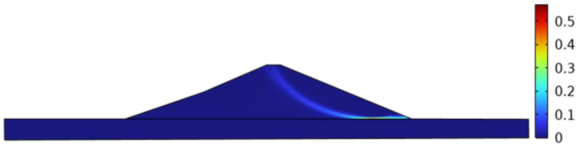

Fig. 7. Plastic strain contour map at normal reservoir level (108.5 m, FoS = 1.92).

The stability evolution during drawdown is then assessed for representative reservoir levels. The critical plastic strain contours together with the computed FoS values are compiled in Fig. 8. Across all drawdown cases, a curved plastic shear band develops on the downstream side at the limit state. Moreover, the plastic strain intensity and affected area increase as the water level decreases, indicating progressive stability deterioration. The FoS values decrease notably with drawdown: 1.94 at 106 m, 1.88 at 103 m, 1.68 at 102.5 m, 1.42 at 102 m, 1.22 at 101.5 m, and 1.02 at 101 m.

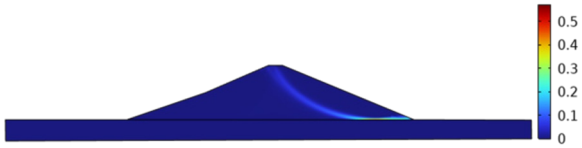

(a) Water level at 106 m (FoS=1.94)

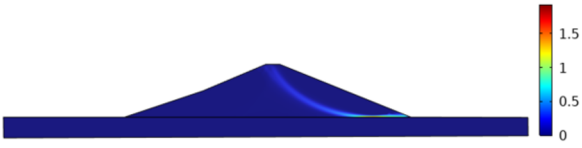

(b) Water level at 103 m (FoS=1.88)

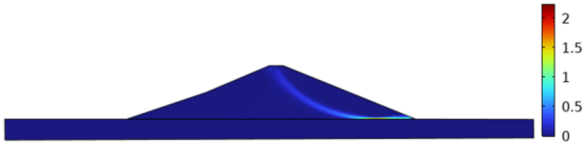

(c) Water level at 102.5 m (FoS=1.68)

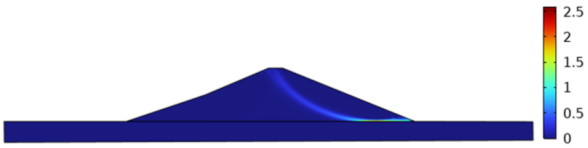

(d) Water level at 102 m (FoS = 1.42)

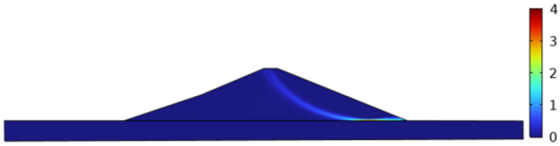

(e) Water level at 101.5 m (FoS = 1.22)

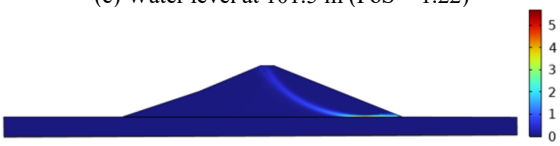

(f) Water level at 101 m (FoS=1.02)

Fig. 8. Plastic strain contour maps and safety factors corresponding to different water levels when the normal reservoir level (108.5 m) is lowered.

The relationship between FoS and reservoir level is further summarized in Fig. 9. A slight FoS increase is observed at the early stage (from 1.92 to 1.96), followed by a rapid decrease to 1.02 as drawdown continues. This non-monotonic behavior can be interpreted in two stages. Initially, the reduction of upstream hydrostatic pressure decreases the external loading effect, leading to a limited change or a slight increase in FoS. As drawdown proceeds, the phreatic surface migrates downward and extends toward the downstream side. The downstream zone becomes increasingly wetted, which reduces suction-related strength contribution and decreases shear strength. At the same time, seepage redistribution produces unfavorable hydraulic gradients within the downstream slope, accelerating the formation of a continuous failure band.

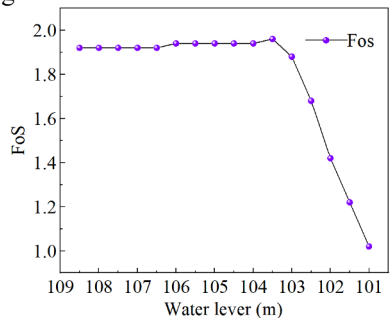

Fig. 9. Safety and stability coefficients of earth-rock dams at different reservoir water levels.

The ultimate failure configuration under the lowest drawdown level is illustrated by the critical slip surface in Fig. 10. At a reservoir level of 101 m, FoS equals 1.02, and the most critical slip surface develops on the downstream side. This observation aligns

with the downstream plastic strain evolution in Fig. 8 and the FoS reduction trend in Fig. 9, indicating that stability degradation during rapid drawdown is governed by hydraulic and strength changes concentrated in the downstream slope region.

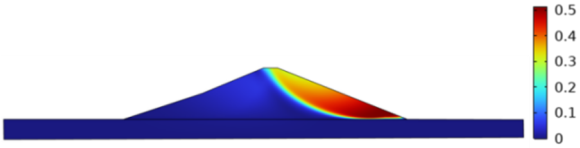

Fig. 10. Failure surface of an earth-rock dam with water level reduced to 101m (FoS=1.02).

The results suggest several operation-oriented implications for small and medium-sized earth dams subjected to rapid water-level changes. First, because the factor of safety decreases rapidly as the reservoir level approaches the lowest drawdown stage in this study, staged drawdown and enhanced surveillance are recommended when low water levels are anticipated or unavoidable. Second, as the critical failure surface predominantly develops on the downstream side, monitoring and inspection should prioritize downstream deformation and pore-pressure response, and the performance of seepage relief and drainage measures should be verified during drawdown operations. Third, the rise scenario produces a broader deformation influence toward the downstream side, indicating that post-storm inspection should include downstream deformation screening to identify potential cumulative effects under alternating rise and drawdown cycles. These recommendations can be integrated with routine monitoring to support operation-oriented safety management.

5 Conclusions

The dam exhibits pronounced transient hydraulic and mechanical responses under reservoir level fluctuations. During rapid drawdown, pore water pressure at upstream slope monitoring points decreases continuously, while effective stress within the dam generally increases, indicating that pore-pressure dissipation induces stress redistribution and elevates the stress carried by the soil skeleton. This coupling highlights the necessity of interpreting stability together with transient seepage evolution.

Deformation patterns differ between drawdown and rise scenarios. Drawdown produces displacement concentration near the upstream side, and displacement increases as the water level decreases, reflecting the time-dependent interaction between boundary unloading and internal seepage adjustment. In contrast, rapid water-level rise triggers a more pronounced downstream displacement response over a broader region, suggesting that rising water levels can modify the seepage field and wetted zone across a larger portion of the dam body.

Strength reduction analysis demonstrates that drawdown substantially reduces stability and that the Fos evolves in a non-monotonic manner. As the reservoir level decreases from 108.5 m to 101.0 m, the FoS increases slightly from 1.92 to 1.96 at the early stage and then drops rapidly, reaching 1.02 at 101.0 m. The critical slip surface predominantly develops on the downstream side, indicating a higher susceptibility of

the downstream slope to the development of a continuous failure band under sustained water-level changes.

The analysis was performed using a two-dimensional maximum cross-section model, and possible three-dimensional effects along the dam axis were not considered. Material properties were taken from available engineering data, while parameter uncertainty and calibration using field monitoring data were not explicitly addressed. In addition, the bedrock layer was not included in the computational domain and its influence was represented through boundary conditions, which may affect local hydraulic and mechanical responses. Future work should incorporate uncertainty quantification and monitoring-based calibration, and extend the analysis to three-dimensional modelling where required. Additional external drivers such as rainfall infiltration and heterogeneous zoning can also be incorporated to improve the robustness of operation-oriented safety evaluation.

References

1. M. Y. Xu, R. Pang, and Y. Zhou, “Seepage safety evaluation of high earth-rockfill dams considering spatial variability of hydraulic parameters via subset simulation,” J. Hydrol., vol. 626, Pt. A, pp. 130-261, 2023. https://doi.org/10.1016/j.jhydrol.2023.130261
2. S. Pourbeirak, A. Johari, and F. A. Daneshvar, “Reliability analysis of seepage in earth dam considering saturated-unsaturated flow: A case study,” Comput. Geotech., vol. 191, pp. 107-797, 2026. https://doi.org/10.1016/j.compgeo.2026.107797
3. A. K. Hu, X. Y. Zhang, and Y. J. Li, “Safety risk analysis of earth-rock dams based on the DEMATEL-ISM-ANP coupled model: With Lianghekou hydropower station for example,” Ain Shams Eng. J., vol. 17, no. 3, pp. 104-004, 2026. https://doi.org/10.1016/j.asej.2026.104004
4. D. Q. Li, Q. Kang, and K. Yan, “A dynamic multi-objective inversion framework for seepage parameters based on monitoring data: case study of an earth-rockfill dam,” J. Hydrol., pp. 135-064, 2026. https://doi.org/10.1016/j.jhydrol.2026.135064
5. Y. Li, Y. Ding, Y. Fang, D. Shi, and Q. Xie, “Stability analysis of a gravelly soil slope based on energy criterion and discrete element strength reduction method,” Comput. Part. Mech., vol. 12, no. 5, pp. 3299–3315, 2025. https://doi.org/10.1007/s40571-025-01008-w
6. S. Farooq, H. Ara, M. Imtiaz, and M. H. Helal, “Thermal behavior of Eyring-Powell liquids through porous compliant peristaltic walls under modified Darcy law and thermopherotic velocity,” Therm. Sci. Eng. Prog., vol. 67, pp. 104-168, 2025. https://doi.org/10.1016/j.tsep.2025.104168
7. R. Abbasov, M. Fahs, V. Fontaine, H. M. Baalousha, A. Younes, and R. Toussaint, “Assessing simplified approaches in modeling rainfall-induced landslides using Richards' equation with Biot poroelasticity,” Eng. Geol., vol. 360, pp. 108-481, 2026. https://doi.org/10.1016/j.enggeo.2025.108481
8. Y. Fouad, I. Soltani, C. Cudennec, and D. Michot, “Using near-infrared spectroscopy to estimate soil water retention curves with the van Genuchten model,” Geoderma, vol. 454, pp. 117-175, 2025. https://doi.org/10.1016/j.geoderma.2025.117175
9. M. Hayek, “Analytical solution for steady vertical flux through unsaturated soils based on van Genuchten-Mualem model,” J.Hydrol., vol. 634, pp. 131-066, 2024. https://doi.org/10.1016/j.jhydrol.2024.131066

10. F. B. Fernandes, A. M. B. Braga, A. L. S. de Souza, and A. C. Soares, “Mechanical formation damage control in permeability Biot’s effective stress-sensitive oil reservoirs with source/sink term,” J. Pet. Sci. Eng., vol. 220, Pt. B, pp. 111-180, 2023. https://doi.org/10.1016/j.petrol.2022.111180
11. Y. Sun, J.-B. Colliat, and J. Shao, “3D Enhanced finite element modeling (E-FEM) in hydromechanical coupling: Applications in the fracking of porous media,” Comput. Methods Appl. Mech. Eng., vol. 448, Pt. B, pp. 118-501, 2026. https://doi.org/10.1016/j.cma.2025.118501
12. F. Wang, L. Yuan, Z. Zhan, R. Cheng, T. Li, C. Lin, and S. Pan, “A novel solid-plate coupling finite element method for face slab of concrete-faced rockfill dams,” Comput. Struct., vol. 316, pp. 107-916, 2025. https://doi.org/10.1016/j.compstruc.2025.107916
13. H. Liu, J. Liu, S. Zhang, L. Feng, and L. Qiu, “Experimental study on compression characteristics of fractured soft rock and its Mohr-Coulomb criterion,” Theor. Appl. Fract. Mech., vol. 125, pp. 103-820, 2023. https://doi.org/10.1016/j.tafmec.2023.103820